Electronic properties of semiconducting Ca_2Si silicide: From bulk to nanostructures by means of first principles calculations

2015 Jpn. J. Appl. Phys. 54 07JA03

(http://iopscience.iop.org/1347-4065/54/7S2/07JA03)

Japanese Journal of Applied Physics **54**, 07JA03 (2015) **REVIEW PAPER**
http://dx.doi.org/10.7567/JJAP.54.07JA03

Electronic properties of semiconducting Ca_2Si silicide: From bulk to nanostructures by means of first principles calculations

D. B. Migas[1*], V. O. Bogorodz[1], A. B. Filonov[1], V. L. Shaposhnikov[1], V. E. Borisenko[1], and N. G. Galkin[2,3]

[1]*Belarusian State University of Informatics and Radioelectronics, P. Browka 6, 220013 Minsk, Belarus*
[2]*Institute for Automation and Control Processes of FEB RAS, 5 Radio St., 690041, Vladivostok, Russia*
[3]*Far Eastern Federal University, 8 Sukhanova St., 690900, Vladivostok, Russia*
E-mail: migas@bsuir.by

Received September 29, 2014; accepted January 20, 2015; published online June 11, 2015

Results of our ab initio calculations have revealed changes in electronic properties in Ca_2Si semiconducting silicide when reducing dimensionality from bulk to slabs and, eventually, to nanowires. In the case of the bulk, Ca_2Si is found to be a direct band-gap semiconductor with the band-gap value of 0.30, 0.60, and 0.79 eV by using the generalized gradient approximation, the modified Becke–Johnson exchange potential and the screened hybrid functional, respectively. We have also identified that among Ca_2Si(001), (010), and (100) surfaces the (100) one has the lowest surface energy. Ca_2Si slabs with (010) or (100) surfaces are predicted to be semiconductors, while (001) surface provides metallic properties due to surface states. The role of the surface states in the band-gap variation is also discussed. In the case of Ca_2Si nanowires with ⟨001⟩, ⟨010⟩, and ⟨100⟩ axes and different morphologies only the ⟨001⟩ orientation guarantees semiconducting properties because of absence of {001} facets which induce metallic properties as for the corresponding slab.

1. Introduction

Silicides, which are mainly characterized by metallic properties, have been intensively investigated for several decades because they are compatible with traditional silicon technology and widely used in microelectronics.[1)] Nevertheless, there are several semiconducting silicides[2)] and among them β-$FeSi_2$ has attracted much attention due to its perspectives in thermoelectric[3)] and optoelectronic[4)] applications. In the latter case it is found that a particular shape of β-$FeSi_2$ precipitates in monocrystalline silicon provides 1.54 μm photoluminescence peak, which is produced by indirect transition in precipitates and quenched at room temperature.[5,6)] The maximum value of dimensionless figure of merit ZT is found to be of 0.27 for Mn-doped Ru_2Si_3 crystals[7)] and 0.42 for $MnSi_{1.74+\delta}$ bulk,[8)] the other semiconducting silicides with promising thermoelectric properties. However, such values are not close to 1 or larger than 1 that compromises their application.

Recently, a lot of effort has been concentrated on semiconducting alkaline-earth metal silicides, namely Mg_2Si, Ca_2Si, and $BaSi_2$, which are less investigated with respect to transition metal silicides and their semiconducting properties are sometimes unknown or scarce.[2)] In addition, the semiconducting alkaline-earth metal silicides are environmentally friendly and mostly consist of abundant materials. The measured maximal value of figure of merit ZT has turned out to be close to 1 in $Mg_2Si_{0.9-x}Sn_xGe_{0.1}$ solid solutions.[9)] Ca_2Si can also be considered as a potential candidate for use as an efficient thermoelectric material. For example, the Ca_2Si experimentally measured Seebeck coefficient of about 300 mV/K is quite comparable with the one of Ru_2Si_3 over the temperature range of 373 to 573 K.[12)] Moreover, it is shown that Mg- and Ca-based intermetallic compounds can be viewed as new biodegradable implant materials.[10)] Hydrogen absorption measurements indicated pure Ca_2Si to be readily hydridable pointing out perspectives in applications for hydrogen storage.[11,13)]

Ca_2Si crystallizes in a simple orthorhombic structure (the *Pnma* space group) with the lattice parameters summarized in Table I. The primitive cell, which is shown in Fig. 1, includes four formula units, whereas all atoms are grouped into three equal sets of chemically inequivalent sites. Each silicon atom is surrounded by tricapped prisms formed by calcium atoms.[14)]

Table I. Experimentally measured and theoretically calculated lattice parameters (in Å) of orthorhombic Ca_2Si.

	a	*b*	*c*	Reference
Experiment	7.667	4.799	9.002	15
	7.691	4.816	9.035	16
	7.6910	4.8174	9.0477	11
Theory	7.618	4.793	9.001	29
	7.664	4.799	9.002	33
	7.647	4.837	8.990	31
	7.609	4.769	9.880	32
	7.615	4.820	9.051	This work

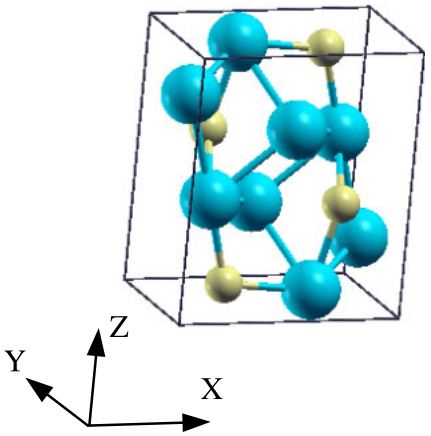

Fig. 1. (Color online) Unit cell of Ca_2Si in the simple orthorhombic structure. Large blue spheres indicate calcium atoms, while small yellow spheres stand for silicon atoms. Crystal axes are also shown.

Experimentally Ca_2Si bulk can be prepared by melting elemental calcium and silicon in closed containers due to the much higher vapor pressure of calcium compared to silicon.[16,17)] Single phase Ca_2Si bulk crystals have been also

grown by the interdiffusion process using Mg_2Si bulk crystals under a calcium vapor where the desolated magnesium atoms were revaporated from the crystal surface through silicide into the vacuum.[18] In addition, single-phase Ca_2Si sintered compacts were synthesized by the spark plasma sintering technique.[12] Even though calcium has a high vapor pressure, Ca_2Si layers have been successfully grown on different silicon substrates[19–21] and Mg_2Si/Si substrates.[19,20,22–24] It is also possible to cover Ca_2Si layers by an amorphous silicon cap that is desirable for silicon planar technology.[23]

According to temperature conductance data the band gap of Ca_2Si bulk is estimated to be 1.9 eV.[25] Semiconducting nature of this silicide has been confirmed by the photoemission[26] and inverse-photoemission[27] experiments. Very recently, temperature-dependent Hall measurements on thin films of Ca_2Si revealed the band-gap value of 1.02 eV.[22] At the same time, results of ab initio calculations mostly predict Ca_2Si to be a semiconductor with the band gap of about 0–1.02 eV. Thus, there is only one band structure obtained by the linear muffin-tin orbital method within the local density approximation indicating semimetal properties,[26] whereas, recent pseudopotential calculations within the generalized gradient approximation unraveled the direct band gap of about 0.31–0.35 eV.[12,28–32] Moreover, quasiparticle calculations within the GW approximation have provided the band-gap value to be the same as experimentally determined by Hall measurements — 1.02 eV.[33] In addition, the detailed description of the density of states and dielectric function of Ca_2Si have been presented in Refs. 29, 31–33.

In this paper we only focus on electronic properties of Ca_2Si and their possible modifications by reducing structural dimensionality from bulk to thin films and eventually to nanowires as predicted by means of ab initio calculations.

2. Computational details and structural models

The structural optimization and band structure calculations of Ca_2Si bulk have been performed by utilizing the first principles total energy projector-augmented wave method (code VASP) described in detail elsewhere.[34–37] Exchange and correlation potentials were included using the generalized gradient approximation of Perdew–Burke–Ernzerhof (PBE).[38] Total energy minimization, via an optimization of the lattice parameters and relaxation of the atomic positions in a conjugate gradient routine, was obtained by calculating the Hellmann–Feynman forces and the stress tensor. The energy cutoff of 400 eV and the $9 \times 13 \times 7$ grid of Monkhorst–Pack points were utilized for the self-consistent procedure. Structural optimization was stopped when forces acting on the atoms were smaller than 0.01 eV/Å. The convergence in the total energy was better than 1 meV per formula unit. The calculation of band structures along some high symmetry directions of the Brillouin zone was performed on the obtained self-consistent charge densities. The charge distributions and transfers have been analyzed by utilizing the Bader method.[43] The effective mass tensors for holes and electrons were evaluated along the principal axes of the ellipsoidal energy surface in the band extrema by calculating the appropriate second derivatives within the five-point approximation.

The calculation of the electronic band structure has also been carried out by means of the self-consistent full potential linearized augmented plane wave method in its scalar-relativistic version using WIEN2k package.[44] The structural parameters of Ca_2Si fully optimized by the projector-augmented wave method have been taken into consideration. We also applied the same PBE generalized gradient approximation.[38] In some cases the modified Becke–Johnson exchange potential[39–41] as well as the screened hybrid functional YS-PBE0 (where YS stands for Yukawa screened)[42] were used to correct band-gap values. Within the muffin-tin spheres, lattice harmonics with angular momentum l up to 10 are used to expand the charge density, potential and wave functions. The muffin-tin radii R_{mt} were set to 2.3 and 2.0 a.u. for calcium and silicon atoms, respectively. We performed the self-consistent procedure with the energy cut-off constant $R_{mt} \cdot K_{max} = 8$ and on meshes of 45 **k**-points in the irreducible part of the Brillouin zone. For calculations with the screened hybrid potential the mesh was 24 **k**-points. Further increase in the cut-off value, basis set and **k**-point number did not lead to any noticeable changes in the eigenvalues. The integration on the Brillouin zone has been carried out by the tetrahedron method with Blöchl corrections. For a band structure representation we choose up to 40 **k**-points for any high-symmetry direction.

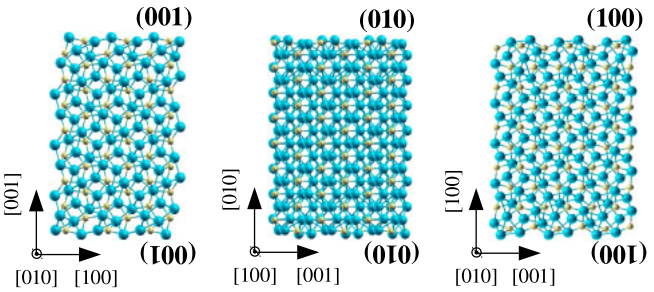

Fig. 2. (Color online) Lateral view of Ca_2Si(001), (010), and (100) slabs with the thicknesses of 3.5, 3.7, and 3.7 nm, respectively. The large, blue spheres indicate calcium atoms while the small, yellow spheres stand for silicon atoms. Crystallographic axes are also indicated.

In the case of slab investigations we have applied the first principles total-energy projector-augmented wave method with plane wave basis set (code VASP) for structural optimization and surface band structure calculations. Exchange and correlation potentials PBE as well as the energy cutoff were kept the same as for the bulk calculations. The Ca_2Si(001), (010), and (100) surfaces have been considered as periodic arrangement of slabs separated by 9 Å of vacuum. This thickness of vacuum is found to be enough to exclude an interaction between the slabs. Each slab is characterized by two equal surfaces. We have considered the slabs with comparable thicknesses of about 3.5 nm obtained by enlarging five, eight, and four times the corresponding a, b, and c lattice parameters of the bulk for the slabs with the (100), (010), and (001) surfaces (as shown in Fig. 2), respectively, and with the (1×1) surface reconstruction (see Fig. 3). All of the atoms in the slab were allowed to relax. To assure convergence, the $1 \times 11 \times 11$ or $11 \times 1 \times 11$ or $11 \times 11 \times 1$ grid of Monkhorst-Park points has been used at final iterations for the slabs with the (100) or (010) or (001) surfaces, respectively. The atomic relaxation was stopped when forces on the atoms were smaller than 0.05 eV/Å. The convergence in the total energy was better than 1 meV per

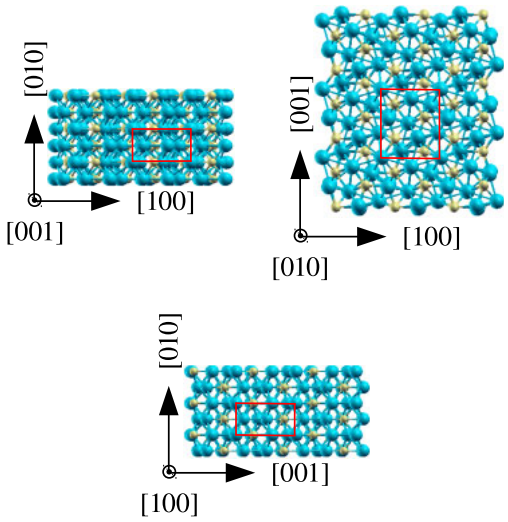

Fig. 3. (Color online) Top view of Ca_2Si(001), (010), and (100) surfaces. The large, blue spheres indicate calcium atoms while the small, yellow spheres stand for silicon atoms. The corresponding (1×1) surface unit cells are marked by red rectangles. Crystallographic axes are also shown.

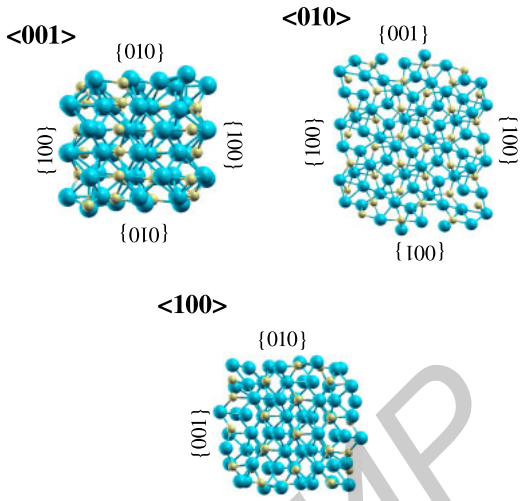

Fig. 4. (Color online) Cross sections of Ca_2Si NWs with the square morphology and diameters of 1.9, 3.2, and 2.2 nm (from top to bottom) after full structural optimization. The large, blue spheres indicate calcium atoms while the small, yellow spheres stand for silicon atoms. NW orientations and facets are indicated.

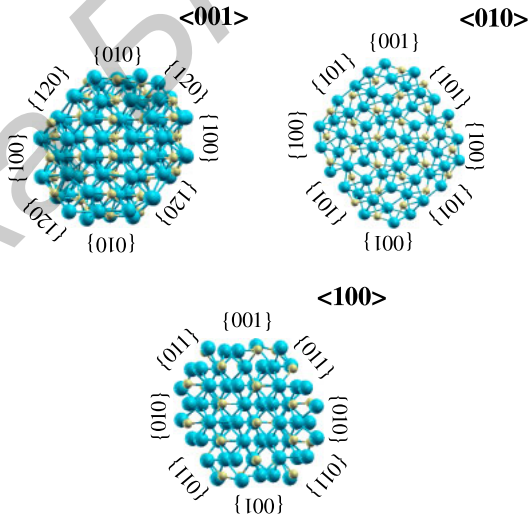

Fig. 5. (Color online) Cross sections of Ca_2Si NWs with the polyhedron morphology and diameters of 1.9, 2.6, and 2.0 nm (from top to bottom) after full structural optimization. The large, blue spheres indicate calcium atoms while the small, yellow spheres stand for silicon atoms. NW orientations and facets are indicated.

formula unit. The calculations of band structures were performed on the self-consistent charge densities. The surface energies of various Ca_2Si surfaces have been calculated as a difference in the total energy between a slab and the bulk (rescaled to the number of formula units as in the corresponding slab) divided by doubled of surface area.

The structural optimization and band structure calculations of Ca_2Si nanowires (NWs) with different orientations have been performed by means of the first principles total energy projector-augmented wave method (code VASP) within the PBE generalized gradient approximation. We have considered ⟨001⟩-, ⟨010⟩-, and ⟨100⟩-oriented Ca_2Si NWs with different cross sections and diameters ranging from 1.9 to 3.2 nm, while periodic boundary conditions have been applied along the nanowire axis with the unit cell parameter ($a_\parallel$). The energy cutoff of 400 eV (as in the cases of bulk and slab calculations) and the grid of $1 \times 1 \times 6$ Monkhorst-Park points were enough to display changes in the total energy difference between various configurations less than 0.003 eV per formula unit. In order to ensure a negligible interaction between neighboring NWs at least 9 Å of vacuum were introduced. All atoms in Ca_2Si NWs were allowed to relax. Atomic relaxation was stopped when forces acting on the atoms were smaller than 0.05 eV/Å. The optimization of $a_\parallel$ was done by gradually increasing/decreasing its value along with the relaxation of the atomic positions until equilibrium was reached. The calculations of band structures were performed using the self-consistent charge densities.

The initial structures of Ca_2Si NWs have been generated on the basis of the specifically oriented bulk structure by cutting it along different atomic planes in order to form facets parallel to the NW axis. According to the selected orientation of NWs, $a_\parallel$ was set at a, b, and c for such nanostructures with ⟨100⟩, ⟨010⟩, and ⟨001⟩ axes, respectively. The Ca_2Si stoichiometry of NWs was kept invariable. One possible NW morphology can be the square with two different facets almost equal in size, which is shown in Fig. 4 for the Ca_2Si NWs with various orientations. Thus, the square morphology is characterized by {100} and {010} facets for Ca_2Si NWs with ⟨001⟩ axes, while for NWs with the ⟨010⟩ orientations {100} and {001} facets are present and, eventually, {010} and {001} facets form shape of ⟨100⟩-oriented NWs. Another considered here morphology can be the polyhedron with multiple facets (Fig. 5), which can be easily obtained by introducing new facets between the adjacent ones in the square morphology.

3. Electronic properties of Ca_2Si bulk

Optimized lattice parameters of the Ca_2Si bulk have turned out to be very close to the experimentally obtained and theoretically predicted (see Table I). The calculated band structure within the PBE generalized gradient approximation is shown in Fig. 6(a). It is evident that Ca_2Si is a direct band-gap semiconductor because the maximum of the valence band and the minimum of the conduction band are located in

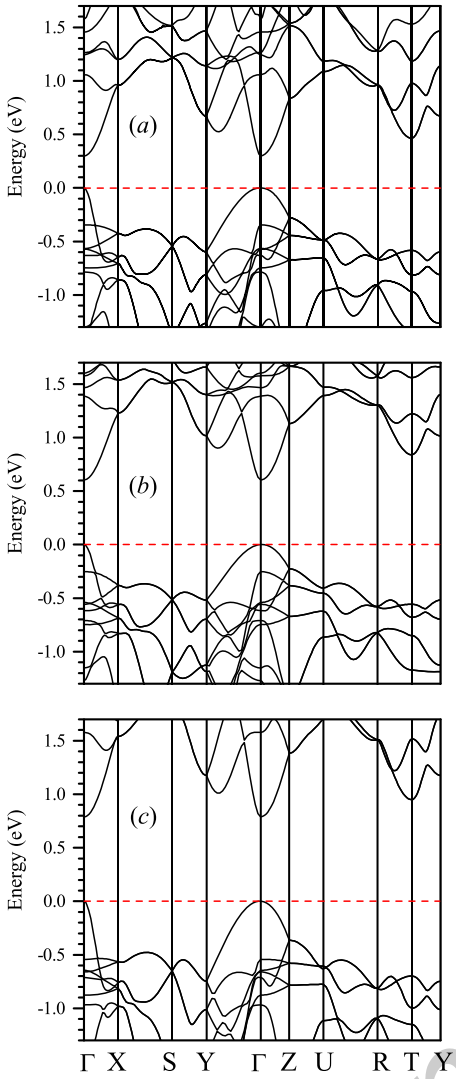

Fig. 6. (Color online) Band structures of Ca_2Si as calculated by utilizing (a) the PBE generalized gradient approximation, (b) the modified Becke–Johnson exchange potential, and (c) the screened hybrid functional YS-PBE0. Zero at the energy scale corresponds to the top of the valence band.

the Γ point. Dispersion of the bands close to the gap region is almost the same as in the previous calculations (see Refs. 12 and 28–33). The d-states of calcium atoms and p-states of silicon atoms can be found in the maximum of the valence band, while the s- and d-states of calcium atoms and d-states of silicon atoms dominate in the minimum of the conduction band. However, the first direct transition is characterized by the very low oscillator strength as determined in recent calculations.[29,33)]

The obtained band-gap value of 0.30 eV is very close to the one predicted in Refs. 12 and 28–32, where the generalized gradient approximation has been used, and such a value is rather small due to well-known band-gap underestimation with respect to the experimentally determined one (1.02 eV) by Hall measurements[22)] and to the theoretically estimated one (1.02 eV) by means of quasiparticle calculations.[33)] We have decided to implement the modified Becke–Johnson exchange potential, which can improve estimates of band-gap values. In fact, the gap of 0.60 eV has been obtained for Ca_2Si [see Fig. 6(b)], whereas the band dispersion near the gap region is very similar to the one presented in Fig. 2(a). Moreover, by using the screened hybrid functional the band-gap value is further increased up to 0.79 eV [Fig. 6(c)].

Table II. The components of the effective-mass tensor (m_1, m_2, m_3) for holes and electrons for the Ca_2Si bulk expressed in units of free-electron mass.

Holes	Electrons
2.30	0.10
2.13	0.63
0.15	0.75

We have also calculated the effective masses of holes and electrons in the maximum of the valence band and in the minimum of the conduction band, which are both located in the Γ point (see Fig. 6). They are summarized in Table II pointing out that the effective masses of holes are larger than the ones of electrons. For the sake of comparison, the effective masses of holes are sizably smaller and comparable to the ones of electrons for β-$FeSi_2$[6)] and $BaSi_2$,[45)] respectively. In the case of the other semiconducting calcium silicide (Ca_3Si_4) some components of the effective mass tensor are significantly larger because of peculiarities in its band structure.[46)] Moreover, accounting for the fact that Ca_2Si showed a p-type conductivity over a rather wide temperature range,[12)] one can suggest the strong anisotropy in the transport and thermoelectric properties of the material according to the significant difference in the components of the hole effective tensor.

By implementing the Bader analysis, we have estimated charge distribution among atoms in Ca_2Si bulk. It was revealed that calcium atoms donated 1.24–1.30e^- while each silicon atom accepted 2.54e^-. It is evident that the charge transfer is larger than 1e^- indicating mostly ionic nature of chemical bonding, while the corresponding values are comparable or even larger than that of the TiO_2 bulk, nanowires and nanotubes both in the rutile[47)] and anatase[48,49)] phases.

4. Electronic properties of Ca_2Si slabs

The lateral and top views of Ca_2Si slabs with (001), (010), and (100) surfaces are shown in Figs. 2 and 3, respectively. The Ca_2Si(001) and (100) surfaces contain calcium atoms in the topmost layer, while silicon atoms are situated slightly below. In the case of the Ca_2Si(010) surface both calcium and silicon atoms form the topmost layer. We have also notice that atomic relaxation does not sizably reshuffle atoms close to the surface. Thus, the Ca–Si interatomic distances of the first neighbors at the surface get shorter by 2–6% mainly for the Ca_2Si(001) and (010) surfaces along with increasing of the thickness of the slabs (by 1–2%) after optimization. Contrary to that, very light changes can be spotted in first neighbor distances for the Ca_2Si(100) surface and the thickness of the slabs slightly shrinks (by 2%). The Bader analysis of charge transfer between atoms has revealed comparable values as in the case of the bulk for the Ca_2Si(010) and (100) slabs. Only for the Ca_2Si(001) slabs some surface calcium and silicon atoms respectively donate and accept less charge (1e^- and 2.1e^-).

We have also estimated surface energies for the Ca_2Si(001), (010), and (100) surfaces, which are summarized in Table III, indicating Ca_2Si(100) to be the most thermody-

Table III. The surface energies (in meV/Å)^2 for different Ca_2Si surfaces.

Surface	(001)	(010)	(100)
Surface energy	70.7	49.2	44.0

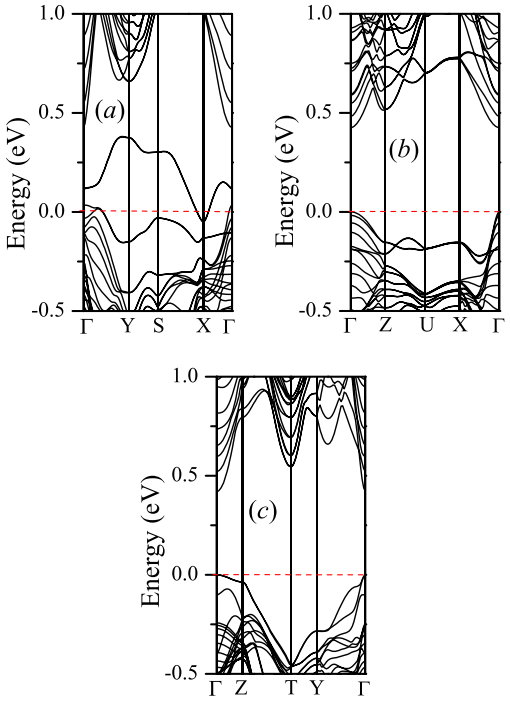

Fig. 7. (Color online) Band structures of the Ca_2Si slabs with (a) the (001), (b) the (010), and (c) the (100) surfaces. Zero at the energy scale corresponds to the top of the valence band for the Ca_2Si slabs with the (010) and (100) surfaces, while for the Ca_2Si slabs with the (001) surfaces it indicates the Fermi level.

namically preferable surface. The surface energy values are smaller with respect to different silicon and germanium surfaces.[50] This issue can be explained by the ionic chemical bonding in Ca_2Si, where surface calcium atoms due to the charge transfer virtually get rid of some dangling bonds. While in the case of silicon and germanium, materials with typical covalent banding, dangling bonds are unavoidably present. The sizable difference in surface energy between the Ca_2Si(001) and (100) surfaces (see Table III) can be attributed to the elastic effects because of changes in bond lengths of the surface atoms as discussed above.

The corresponding band structures of the Ca_2Si slabs with (001), (010), and (100) surfaces are presented in Fig. 7. For simplicity reason the labeling of the high symmetry points in the surface Brillouin zone was preserved as in the bulk case. It is clearly seen that the Ca_2Si(001) slab can be considered as a metal since the Fermi level crosses some bands [Fig. 7(a)] even though there is an energy gap laying slightly higher in energy. We have traced atoms whose states populated the bands at the Fermi level energy. All of them, both calcium and silicon, have turned out to be from the surface and subsurface regions, as indicated in Fig. 8, whereas mostly calcium p- and d-states with a slight admixture of s-states and silicon p-states can be found at this energy. Moreover, a separate band laying just above the Fermi level energy can be viewed as a surface state. On the contrary, the Ca_2Si(010) and (100) slabs do not display metallic properties [Figs. 7(b) and 7(c)], whereas dispersion of the top valence band and of the

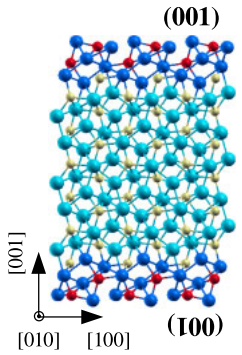

Fig. 8. (Color online) Lateral view of the Ca_2Si(001) slabs highlighting calcium (large, dark blue spheres) and silicon (small, red spheres) atoms which have their states at the Fermi level. The rest of the calcium and silicon atoms are large, blue and small, yellow spheres, respectively.

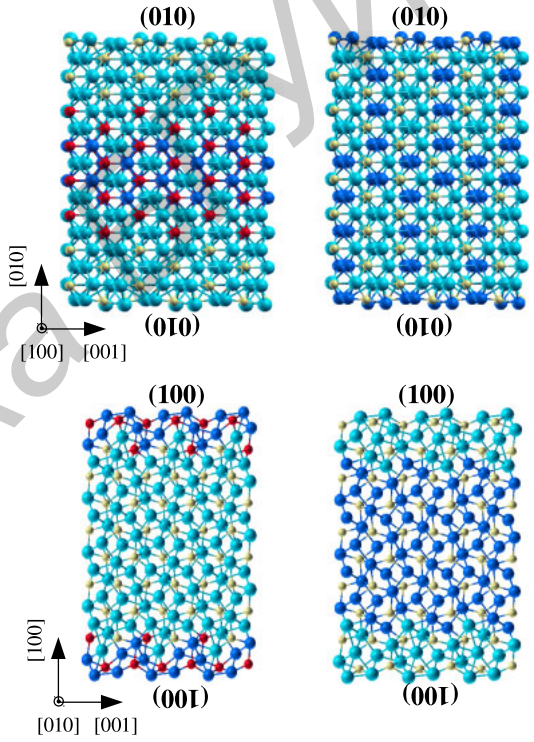

Fig. 9. (Color online) Lateral view of the Ca_2Si(010) and (100) slabs highlighting calcium (large, dark blue spheres) and silicon (small, red spheres) atoms whose states characterize the top of the valence band (the left panel) and the bottom of the conduction band (the right panel). The rest of the calcium and silicon atoms are large, blue and small, yellow spheres, respectively.

bottom conduction band resembles the one of the bulk (see Fig. 6) with well-pronounced valence band maximum and conduction band minimum in the Γ point. For the Ca_2Si(010) the maximum of the valence band is defined by d-states of calcium atoms and p-states of silicon atoms located in the inner part of the slab, while s- and d-states of calcium atoms spread all over the slab characterize the minimum of the conduction band (Fig. 9). In the case of the Ca_2Si(100) slab the maximum of the valence band again has p- and d-states of calcium atoms and p-states of silicon atoms but these atoms can be spotted in the surface region. Only calcium atoms, which are situated in the middle part of the slab, contribute their s- and d-states to the minimum of the conduction band. Thus, hole and electron surface states, which are define the

maximum of the valence band and the minimum of the conduction band, are possible for the $Ca_2Si(100)$ and (010) slabs, respectively.

It should be noted here that the considered slabs have a rather high surface-to-volume ratio and surface states can define the top of the valence band and/or the bottom of the conduction band, as well as lead to metallic properties. By increasing thickness of these slabs the surface-to-volume ratio gets smaller and, as a result, surface states should be treated as common surface states. Similar effects have been already discussed by some of us for TiO_2 NWs.[48,49)]

The estimated band gaps for the $Ca_2Si(100)$ and (010) slabs are about 0.48 eV that is larger than for the bulk due to quantum confinement effects. Nevertheless, we do not expect the band gap (E_g) to change according to a common $E_g \sim 1/d^2$ law, where d is the thickness of a slab, because of the surface states. The surface states, providing significant contribution to the maximum of the valence band and/or the minimum of the conduction band, are not affected by quantum confinement effects and, as a result, a band gap variation can be blocked. The influence of the surface states on band-gap values has been already carefully investigated in the case of TiO_2 nanowires and nanotubes.[48,49,51)]

5. Electronic properties of Ca_2Si NWs

After structural optimization the shape of Ca_2Si NWs is not sizably changed with respect to "as-cut" initial structure. We have noticed that surface atoms on facets behave as the ones on the corresponding surfaces in slabs mainly leading to decreasing in the Ca–Si interatomic distances for the first neighbors. Moreover, changes in $a_{\parallel}$ are found to be marginal.

Since the $Ca_2Si(001)$ surface has displayed metallic properties due to the appearance of surface states in the gap region (see Figs. 7 and 8), it is highly expected that such surface states are also transferable onto NWs. In fact, the band structures of ⟨010⟩- and ⟨100⟩-oriented Ca_2Si NWs independently of morphology indeed show the Fermi level to cross several bands (see Fig. 10). We have identified atoms contributing their states to these bands. Thus, p- and d-states of calcium atoms and p-states of silicon atoms belonging to {001} facets can be traced. Contrary to the ⟨010⟩- and ⟨100⟩-oriented Ca_2Si NWs, NWs with ⟨001⟩ axes preserve semiconducting properties. Nevertheless, some empty bands appear in the gap region, which are associated with d-states of surface calcium atoms located at edges between adjacent {100} and {010} or {120} facets. Because of these separate bands, acting as surface states and as the minimum of the conduction band, the band-gap value is even smaller than in the bulk.

6. Conclusions

Our ab initio predictions on electronic properties of Ca_2Si bulk agree well with previous theoretical calculations that this silicide is a direct band-gap semiconductor. We also show the modified Becke–Johnson exchange potential and the screened hybrid functional YS-PBE0 to improve the band-gap value (0.60 and 0.79 eV, respectively), however its estimate is still smaller than experimental data (1.02 eV) and obtained by quasiparticle calculation (1.02 eV). Evaluation of effective masses indicates effective masses of holes to be as twice as larger than the ones of electrons. Surface energy

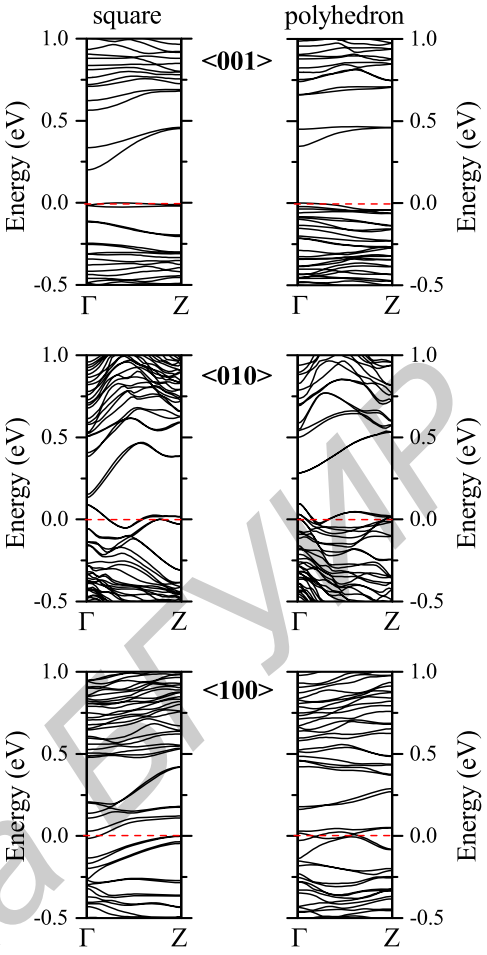

Fig. 10. (Color online) Band structures of Ca_2Si NWs with different orientations and morphologies which are indicated. Zero at the energy scale corresponds to the top of the valence band for the ⟨001⟩-oriented Ca_2Si NWs and to the Fermi level for the ⟨010⟩- and ⟨100⟩-oriented Ca_2Si NWs.

calculations have identified that the most thermodynamically preferable surface is $Ca_2Si(100)$, whereas the surface energy is sizably smaller in comparison with any silicon or germanium surface. Band structures of Ca_2Si slabs have manifested metallic properties only in the case of the (001) surface because of the appearance of surface states in the gap region, while slabs with the (010) and (100) surfaces are direct band-gap semiconductors. We have also discussed that quantum confinement effects can be attenuated if the maximum of the valence band and/or the minimum of the conduction band are defined by states of surface atoms that is the case of $Ca_2Si(010)$ and (100) slabs. Ca_2Si NWs with ⟨100⟩ and ⟨010⟩ orientations also display surface states in the gap region leading to metallic properties independently of morphology. At the same time, Ca_2Si NWs with ⟨001⟩ axes are semiconductors because of the absence of {001} facets. We believe that metallic properties of Ca_2Si slabs and NWs can be switched to semiconducting ones by saturating surface dangling bonds by hydrogen.

Acknowledgment

D.B.M. is grateful to the organizers of the International Conference and Summer School on Advanced Silicide Technology 2014 (ICSS-SILICIDE 2014) for a kind invitation and a nice opportunity to present recent results on silicides.

1) *Properties of Metal Silicides*, ed. K. Maex and M. van Rossum (Inspec, London, 1995).
2) *Semiconducting Silicides*, ed. V. E. Borisenko (Springer, Berlin, 2000).
3) A. Heinrich, in *Silicides: Fundamentals and Applications*, ed. L. Miglio and F. d'Heurle (World Scientific, Singapore, 2000) p. 126.
4) D. N. Leong, M. A. Harry, K. J. Reeson, and K. P. Homewood, Nature **387**, 686 (1997).
5) M. G. Grimaldi, C. Buongiorno, C. Spinella, E. Grilli, L. Martinelli, M. Gemelli, D. B. Migas, L. Miglio, and M. Fanciulli, Phys. Rev. B **66**, 085319 (2002).
6) L. Martinelli, E. Grilli, D. B. Migas, L. Miglio, F. Marabelli, C. Soci, M. Geddo, M. G. Grimaldi, and C. Spinella, Phys. Rev. B **66**, 085320 (2002).
7) A. E. Krivosheev, L. I. Ivanenko, A. B. Filonov, V. L. Shaposhnikov, G. Behr, J. Schumann, and V. E. Borisenko, Semiconductors **40**, 27 (2006).
8) T. Yamada and H. Yamane, Phys. Status Solidi C **10**, 1692 (2013).
9) S. Tada, Y. Isoda, H. Udono, H. Fujiu, S. Kumagai, and Y. Shinohara, Phys. Status Solidi C **10**, 1704 (2013).
10) K. Hagihara, K. Fujii, A. Matsugaki, and T. Nakano, Mater. Sci. Eng. C **33**, 4101 (2013).
11) H. Wu, W. Zhou, T. J. Udovic, and J. J. Rush, J. Alloys Compd. **446–447**, 101 (2007).
12) C. Wen, T. Nonomura, A. Kato, Y. Kenichi, H. Udono, K. Isobe, M. Otake, Y. Kubota, T. Nakamura, Y. Hayakawa, and H. Tatsuoka, Phys. Procedia **11**, 106 (2011).
13) H. Wu, W. Zhou, T. J. Udovic, and J. J. Rush, Chem. Mater. **19**, 329 (2007).
14) A. K. Ganguli, A. M. Guloy, and J. D. Corbett, J. Solid State Chem. **152**, 474 (2000).
15) P. Eckerlin and E. Woller, Z. Anorg. Chem. **280**, 321 (1955).
16) P. Manfrinetti, M. L. Fornasini, and A. Palenzona, Intermetallics **8**, 223 (2000).
17) A. Palenzona, P. Manfrinetti, and M. L. Fornasini, J. Alloys Compd. **312**, 165 (2000).
18) N. Takagi, Y. Sato, T. Matsuyama, H. Tatsuoka, M. Tanaka, C. Fengmin, and H. Kuwabara, Appl. Surf. Sci. **244**, 330 (2005).
19) H. Matsui, M. Kuramoto, T. Ono, Y. Nose, H. Tatsuoka, and H. Kuwabara, J. Cryst. Growth **237–239**, 2121 (2002).
20) H. Tatsuoka, N. Takagi, S. Okaya, Y. Sato, T. Inaba, T. Ohishi, A. Yamamoto, T. Matsuyama, and H. Kuwabara, Thin Solid Films **461**, 57 (2004).
21) T.-W. Pi, C.-P. Cheng, and G. K. Wertheim, J. Appl. Phys. **109**, 043701 (2011).
22) S. A. Dotsenko, D. V. Fomin, K. N. Galkin, D. L. Goroshko, and N. G. Galkin, Phys. Procedia **11**, 95 (2011).
23) L. Dózsa, G. Molnár, Z. Zolnai, L. Dobos, B. Pécz, N. G. Galkin, S. A. Dotsenko, D. A. Bezbabny, and D. V. Fomin, J. Mater. Sci. **48**, 2872 (2013).
24) C. Wen, A. Kato, T. Nonomura, and H. Tatsuoka, J. Alloys Compd. **509**, 4583 (2011).
25) G. Busch, P. Junod, U. Katz, and U. Winkler, Helv. Phys. Acta **27**, 193 (1954).
26) O. Bisi, L. Braicovich, C. Carbone, I. Lindau, A. Iandelli, G. L. Olcese, and A. Palenzona, Phys. Rev. B **40**, 10194 (1989).
27) C. Chemelli, M. Sancrotti, L. Braicovich, F. Ciccacci, O. Bisi, A. Iandelli, G. L. Olcese, and A. Palenzona, Phys. Rev. B **40**, 10210 (1989).
28) Y. Imai and A. Watanabe, Intermetallics **10**, 333 (2002).
29) D. B. Migas, L. Miglio, V. L. Shapohnikov, and V. E. Borisenko, Phys. Rev. B **67**, 205203 (2003).
30) Y. Imai, A. Watanabe, and M. Mukaida, J. Alloys Compd. **358**, 257 (2003).
31) Z. Yang, D. Shi, B. Wen, R. Melnik, S. Yao, and T. Li, J. Solid State Chem. **183**, 136 (2010).
32) Y. Imai, Y. Mori, S. Nakamura, and K. Takarabe, J. Alloys Compd. **558**, 179 (2013).
33) S. Lebègue, B. Arnaud, and M. Alouani, Phys. Rev. B **72**, 085103 (2005).
34) G. Kresse and J. Hafner, Phys. Rev. B **49**, 14251 (1994).
35) G. Kresse and J. Furthmüller, Phys. Rev. B **54**, 11169 (1996).
36) G. Kresse and J. Furthmüller, Comput. Mater. Sci. **6**, 15 (1996).
37) G. Kresse and J. Joubert, Phys. Rev. B **59**, 1758 (1999).
38) J. P. Perdew, S. Burke, and M. Ernzerhof, Phys. Rev. Lett. **77**, 3865 (1996).
39) F. Tran and P. Blaha, Phys. Rev. Lett. **102**, 226401 (2009).
40) D. Koller, F. Tran, and P. Blaha, Phys. Rev. B **83**, 195134 (2011).
41) A. D. Becke and E. R. Johnson, J. Chem. Phys. **124**, 221101 (2006).
42) F. Tran and P. Blaha, Phys. Rev. B **83**, 235118 (2011).
43) W. Tang, E. Sanville, and G. Henkelman, J. Phys.: Condens. Matter **21**, 084204 (2009).
44) P. Blaha, K. Schwarz, G. K. H. Madsen, D. Kvasnicka, and J. Luitz, WIEN2k, An Augmented Plane Wave + Local Orbitals Program for Calculating Crystal Properties (Karlheinz Schwarz, Tech. Universität Wien, Vienna, 2001).
45) D. B. Migas, V. L. Shaposhnikov, and V. E. Borisenko, Phys. Status Solidi B **244**, 2611 (2007).
46) D. B. Migas, V. L. Shaposhnikov, A. B. Filonov, N. N. Dorozhkin, and V. E. Borisenko, J. Phys.: Condens. Matter **19**, 346207 (2007).
47) R. A. Evarestov, D. B. Migas, and Y. F. Zhukovskii, J. Phys. Chem. C **116**, 13395 (2012).
48) D. B. Migas, A. B. Filonov, V. E. Borisenko, and N. V. Skorodumova, Phys. Chem. Chem. Phys. **16**, 9479 (2014).
49) D. B. Migas, A. B. Filonov, V. E. Borisenko, and N. V. Skorodumova, Phys. Chem. Chem. Phys. **16**, 9490 (2014).
50) D. B. Migas, S. Cereda, F. Montalenti, and L. Miglio, Surf. Sci. **556**, 121 (2004).
51) D. B. Migas, V. L. Shaposhnikov, V. E. Borisenko, and F. Arnaud d'Avitaya, J. Phys. Chem. C **114**, 21013 (2010).